Applied Catalysis B: Environmental 144 (2014) 644–653

Contents lists available at ScienceDirect

Applied Catalysis B: Environmental

journal homepage: www.elsevier.com/locate/apcatb

Preparation, photocatalytic activity, and mechanism of $Cd_2Sb_2O_{6.8}$-graphene composite

Peixian Wang, Jiangjun Xian, Jing Chen, Yunhui He, Jinxiu Wang, Wenjuan Li, Yu Shao, Danzhen Li*

Research Institute of Photocatalysis, State Key Laboratory Breeding Base of Photocatalysis, Fuzhou University, Fuzhou 350002, PR China

ARTICLE INFO

Article history:
Received 5 May 2013
Received in revised form 21 July 2013
Accepted 28 July 2013
Available online 7 August 2013

Keywords:
Photocatalysis
$Cd_2Sb_2O_{6.8}$
Graphene
Active species
Nanocomposite

ABSTRACT

Novel nanocomposite materials, based on graphene (GR) and $Cd_2Sb_2O_{6.8}$, were synthesized successfully through a facial one-step hydrothermal method for the first time. Characterized by X-ray diffraction, UV–vis diffuse reflectance spectroscopy, transmission electron microscopy, field emission scanning electron microscopy (FESEM), Fourier-transform infrared spectroscopy, Raman spectroscopy, etc., it demonstrated that $Cd_2Sb_2O_{6.8}$ nanoparticles were effectively anchored in GR sheets. By the degradation of rhodamine B (RhB) and methylene blue, such $Cd_2Sb_2O_{6.8}$-GR nanocomposites exhibited a much higher photocatalytic activity than the pure $Cd_2Sb_2O_{6.8}$. Especially, when the mass ratio of GR in $Cd_2Sb_2O_{6.8}$-GR nanocomposite was 2% (labeled as $Cd_2Sb_2O_{6.8}$-2%GR), it possessed the optimal photocatalytic ability on the degradation of RhB which was as high as that of commercial P25. It was proved that GR played an important role in the enhancement of photocatalytic performance of composites. Which give a good chance to make an effective charge separation and generation of multifarious reactive species, such as $^{\bullet}OH$, $^{\bullet}O_2^-$, h^+, e^-. A possible mechanism of the degradation process was carefully discussed. This work provided a new insight into the photocatalytic degradation of dyes under UV irradiation and opens up a new prospect to $Cd_2Sb_2O_{6.8}$-GR photocatalysts.

1. Introduction

In the past ten years, as an n-type semiconductor, $Cd_2Sb_2O_{6.8}$ has been reported to be sensitive to several gases, such as C_2H_2, trimethylamine (TMA), liquid petrol gas (LPG) and acetone and exhibited especially sensitivity and selectivity toward C_2H_2 [1–3]. Subsequent works enhanced its gas-sensing properties such as sensitivity, selectivity and operating condition by modification and doping [4,5]. Moreover, its gas-sensing mechanism was researched and proved to belong to the surface resistance control by Xingqin Liu groups [6]. However, little research had been done on the photocatalytic ability of $Cd_2Sb_2O_{6.8}$ for degradation of organic pollutants. Our group have reported that the $Cd_2Sb_2O_{6.8}$ nanoparticles have photocatalytic ability toward the degradation of benzene vapor and dyes under UV irradiation [7]. We have prepared pure $Cd_2Sb_2O_{6.8}$ nanocomposites for degradation of organic dyes under UV ($\lambda = 254$ nm) irradiation. The results showed that 150 mL (2×10^{-5} mol/L) rhodamine B (RhB) can be almost decomposed within 60 min irradiation by pure $Cd_2Sb_2O_{6.8}$ nanoparticles, but the mineralization ratio of RhB was very low. Apparently, its ability of photodegradation was not good enough and needed further improvement. And also, the detailed mechanisms of the photocatalytic degradation process based on $Cd_2Sb_2O_{6.8}$ nanoparticles were still vacant.

There has been an explosion of interest in the use of graphene (GR) for the development of new purposes, such as optoelectronics [8,9], chemical and biosensors [10], H_2 production and storage [11–13], supercapacitors [14,15], photovoltaincs and polymer composites [16–19]. These interests were partly motivated by the excellent intrinsic properties of GR including the high mobility of charge carriers, large specific surface area, excellent thermal conductivity and the optical transmittance abilities [20]. These unusual properties made it can be utilized as supporting materials to disperse and stabilize nanocrystals for potential applications of materials. During the past few years, photocatalyst based on GR compounds have been attracting even-increasing enthusiasm, in the aspects of nonselective degradation of pollutants [21–23], photocatalytic selective organic transformations and photocatalytic water splitting to produce hydrogen energy [24–27].

In order to improve the photocatalytic activity of $Cd_2Sb_2O_{6.8}$ nanoparticles and to discuss the specific roles of GR on improving the photocatalytic activities and the possible mechanism of photocatalytic degradation, we prepared $Cd_2Sb_2O_{6.8}$-GR nanocomposites through a facial one-step hydrothermal method for the first time. Due to the introduction of GR, the synthesized $Cd_2Sb_2O_{6.8}$-GR exhibited a higher mineralization ratio and stability than that

* Corresponding author. Tel.: +86 591 83779256; fax: +86 591 83779256.
E-mail addresses: dzli@fzu.edu.cn, danzli@126.com (D. Li).

0926-3373/$ – see front matter © 2013 Elsevier B.V. All rights reserved.
http://dx.doi.org/10.1016/j.apcatb.2013.07.063

of pure $Cd_2Sb_2O_{6.8}$. Moreover, this work provides a basic research for application by combining the advantages of both GR and semiconductors. The role GR played in the system was carefully verified and then a possible mechanism of photocatalytic degradation of RhB process over $Cd_2Sb_2O_{6.8}$-GR nanocomposites was proposed first.

2. Experimental

2.1. Catalyst preparation

All of the reagents were analytical-grade without further purification. The major chemical agents used in this work were as follows. Natural graphite with the particle size range from 45 μm to 500 μm was bought from Qingdao Haida Graphite Co., Cadmium acetate ($C_4H_6CdO_4{\cdot}2H_2O$) and Potassium pyroantimonate ($KSbO_6H_6$) were purchased from Aladdin chemistry Co. Deionized water was used for the preparation of all solutions.

The method of manufacturing $Cd_2Sb_2O_{6.8}$-graphene ($Cd_2Sb_2O_{6.8}$-GR) nanocomposites: (a) the preparation of graphene oxide (GO) was according to a modified Hummers' method (supporting information) [28]. (b) The photocatalyst of $Cd_2Sb_2O_{6.8}$-GR nanocomposites with different GR contents (1 wt%, 2 wt%, 5 wt%) were synthesized via a hydrothermal method by reference our previous work [7]. $KSbO_6H_6$ and $C_4H_6CdO_4{\cdot}2H_2O$ were first dissolved in distilled water to form 0.1 mol/L solutions, respectively. In a typical procedure, GO (7 mg/mL) with a given amount was added into 120 mL of $KSbO_6H_6$ solution with modest stirring followed by ultrasonic treatment for 30 min to form a uniform suspension. Then, 120 mL $C_4H_6CdO_4{\cdot}2H_2O$ solution was slowly dropped into the suspension under continuous stirring. The pH value of the mixture was adjusted to 12 by using ammonia, after which, 10 mL of hydrazine was added to the above suspension. The resulting mixture was loaded into 100 mL Teflon-lined stainless steel autoclave and heated to 180 °C for 24 h under autogenous pressure. After cooling to room temperature naturally, the precipitate was filtered, washed with distilled water for several times and fully dried at 333 K. The final $Cd_2Sb_2O_{6.8}$-GR nanocomposites with different weight addition ratios of GR were named $Cd_2Sb_2O_{6.8}$-1%GR, 2%GR and 5%GR respectively. For comparison, the same method was used to synthesize pure $Cd_2Sb_2O_{6.8}$ without GR.

2.2. Catalyst characterization

The phase constitutions of products were measured by X-ray Diffraction (XRD) on a Bruker D8 Advance X-ray diffractometer with Ni-filtered Cu Ka radiation. The optical properties of the samples were detected by diffuse reflectance spectroscopy (DRS) using a UV–vis Spectrophotometer (Carry-500, Varian CO.) with $BaSO_4$ as the background ranging from 200 to 800 nm. The Transmission Electron Microscopy (TEM) and High-resolution Transmission Electron Microscopy (HRTEM) images were obtained using a FEI Tecnai G2 F20 instrument operated at an accelerating voltage of 200 kV. Field Emission Scanning Electron Microscopy (FESEM) was used to obtain the SEM images on a FEI Nova NANOSEM 230 Spectrophotometer. The Brunauer–Emmett–Teller (BET) specific surface area of the samples were analyzed by nitrogen adsorption at 77 K on an Autosorb-1C-TCD physical adsorption instrument (American Quantach-rome) using a Micrometrics ASAP 2020 system. Fourier-transform Infrared Spectroscopy (FT-IR) analyses were carried out on a Nicolet Avatar 670 FI-IR spectrometer (Nicolet Corp., USA). Absorption bands were observed from 4000 to 500 cm^{-1} with 64 samples scans and 4.0 cm^{-1} resolution. X-ray photoelectron spectroscopy (XPS) analysis was carried out on an ESCALAB 250 photoelectron spectrometer (Thermo Fisher Scientific) at 3.0×10^{-10} mbar with monochromatic Al Kα radiation (E = 1486.2 eV). Shimadzu TOC-VCpH total organic carbon analyzer was used to detect the total organic carbon (TOC) values of catalysts. Raman spectroscopy was recorded at room temperature on a Renishaw invia Raman System and equipped with the 785 nm line of an Ar ion laser as an excitation source. To detect the generation of activated species, Electron spin resonance (ESR) signal-trapped by 5,5-dimethyl-l-pyrroline-N-oxide (DMPO) was collected by a Bruker model A300 spectrometer (Bruker Instruments, Inc.). The settings for the ESR were as follows: center field (3512.48 G), Microwave frequency (9.86 GHz) and Microwave power (20 mw). We use a laser of 254 nm as the light source. The photoelectrochemical experiment was carried out in a three-electrode quartz cell, and used a CHI-660D electrochemical workstation (CH Instruments, USA). The cell was filled with 0.1 mol/L of Na_2SO_4 electrolyte (30 mL). A platinum wire was used as the counter electrode and an Ag/AgCl electrode was used as the reference electrode, while the working electrode was prepared on Indium Tin Oxide (ITO) conducting glass. Generally, the sample powder (20 mg) was ultra-sonicated in 1 mL ethanol to get uniform slurry. The slurry was deposited as a 5 mm × 5 mm film on ITO glass and dried overnight under ambient conditions.

The product formation was measured by liquid chromatography mass/spectrometry (LC-MS) using Trap XCT with electrospray ionization (ESI) interface. The mobile phase consisting of methanol/0.1% acetic acid, and the volume percent of methanol was increased from 35% to 80% within 15 min. The oxidation reduction potential (ORP) and conductivity tests were monitored by an ORP electrode (ORION 9678BNWP) and conductivity cell (ORION 013605MD), respectively. They were all detected on a 5-star meter (Thermo Fisher Scientific Inc.).

2.3. Measurement of photocatalytic activity

The photocatalytic degradations of organic dyes (RhB: 2×10^{-5} mol/L and methylene blue (MB): 2.7×10^{-5} mol/L) in the liquid phase were conducted using a quartz tube reactor system. The system was cooled by a fan cooling system to maintain room temperature and surrounded by four 4-W UV lamps with a wavelength centered at 254 nm (Philips, TUV 4 W/G4 T5). 0.06 g catalysts were loaded into 150 mL of pollutant solution without any addition of acid or alkali. Prior to irradiation, the suspensions were magnetically stirred in dark for 4 h to ensure the establishment of adsorption–desorption equilibrium. After irradiation, 3 mL aliquots were sampled at a certain time interval and centrifuged to remove the catalyst. Then the degraded solutions were analyzed using a Varian UV–vis Spectrophotometer (Carry-50, Varian Co.). The results of degradation reported as C/C_0. C and C_0 were the concentration of pollutant at the momentary and initial times, respectively. For comparison, the photocatalytic activity of P25 was also measured under the same reaction conditions. The mentioned photocatalytic processes in liquid phase in this paper were all measured after the adsorption–desorption equilibrium.

3. Results

3.1. XRD analysis

XRD patterns of pristine graphite (2θ = 26.3°), prepared GO (2θ = 10.8°) and GR (2θ = 25°) were shown in Fig. S1 (Supporting Information). A sharp diffraction peak appearing at 2θ = 10.8° was attributed to GO, indicated that the pristine graphite was oxidized into GO [29]. Another obvious phenomenon was that a weak and broad electron diffraction (2θ = 25°) which belongs to GR.

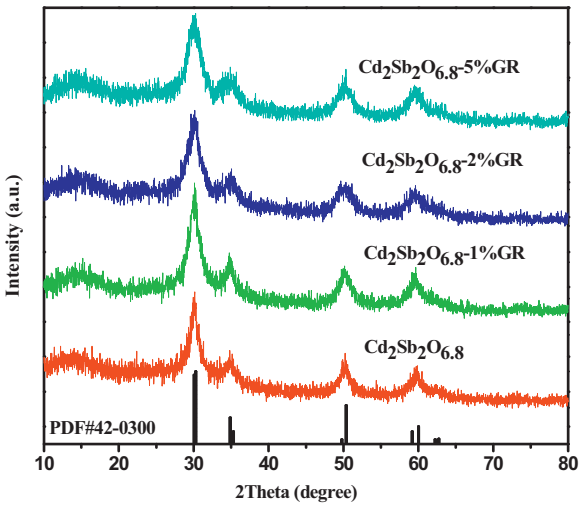

Fig. 1. XRD patterns of the samples prepared at 180 °C for 24 h with different graphene content (pure $Cd_2Sb_2O_{6.8}$, 1%GR, 2%GR, 5%GR).

Fig. 1 shows the XRD patterns of the pure $Cd_2Sb_2O_{6.8}$ and $Cd_2Sb_2O_{6.8}$-GR synthesized at 180 °C for 24 h with different GR contents. It was shown that all diffraction peaks could be assigned to pure phase $Cd_2Sb_2O_{6.8}$ (JCPDS no. 42-0300). Furthermore, four obvious peaks at 30.27°, 34.88°, 50.37° and 59.18° matched well with the (2 2 2), (4 0 0), (4 4 0) and (6 2 2) crystal planes of $Cd_2Sb_2O_{6.8}$ respectively. No impurity was observed in the XRD patterns. XRD patterns of $Cd_2Sb_2O_{6.8}$-GR were as same as the pure $Cd_2Sb_2O_{6.8}$, it was illustrated that the existence of GR did not influence the crystallization of $Cd_2Sb_2O_{6.8}$, which fabricated on GR. However, no typical diffraction peaks corresponding to GR ($2\theta = 25°$) were observed in the XRD pattern for $Cd_2Sb_2O_{6.8}$-GR. This may be ascribe to the fact that during the hydrothermal reaction, GO sheets were reduced to GR (Very weak diffraction peaks belonging to GR, see Fig. S1). On the other hand, the relatively high content (exceed about 95%, W/W) and well crystallinity of $Cd_2Sb_2O_{6.8}$ in $Cd_2Sb_2O_{6.8}$-GR composites revealed stronger diffraction peaks which covered the diffraction of GR [30,31]. To further prove the structure of the nanocomposites, the Raman and IR tests were done in the following part.

3.2. Raman analysis

Raman spectroscopy was a convincing test method used for the characterization of carbon-based materials [32,33]. Raman spectra of $Cd_2Sb_2O_{6.8}$-2%GR and pure $Cd_2Sb_2O_{6.8}$ were shown in Fig. 2.

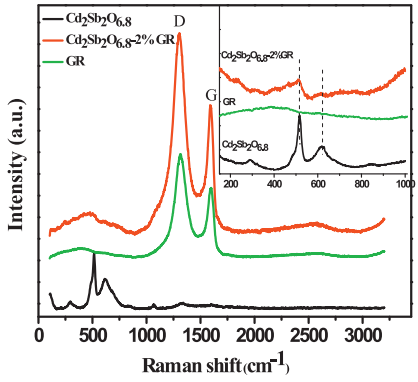

Fig. 2. Raman spectra of $Cd_2Sb_2O_{6.8}$-2%GR, GR and pure $Cd_2Sb_2O_{6.8}$.The spectrum in the inset is a fine scanning to show the characteristic of $Cd_2Sb_2O_{6.8}$ in $Cd_2Sb_2O_{6.8}$-2%GR composite.

The typical Raman features of GO was a strong G band at about 1575 cm^{-1} and a weak D band at approximately 1355 cm^{-1} [33], which belongs to E_{2g} vibration mode in plane and A_{1g} breathing mode, respectively [23]. After GO was reduced to GR, both the G and D bands changed noticeably. The weak D band would reveal to a higher intensity and more wide compared with G band [33]. It indicated a decrease in the average size of the sp^2 domains upon the reduction of GO [23,34]. As shown in Fig. 2, the major peaks at 514 cm^{-1} and 652 cm^{-1} could be attributed to the characteristic band of pure $Cd_2Sb_2O_{6.8}$. It could be evidently seen from the inset that $Cd_2Sb_2O_{6.8}$-2%GR had the characteristic diffraction peaks of pure $Cd_2Sb_2O_{6.8}$, while the Raman spectra of GR was very smooth at 514 cm^{-1} and 652 cm^{-1}. In conclusion, there were both characteristic peaks of $Cd_2Sb_2O_{6.8}$ and GR in the Raman spectrum of $Cd_2Sb_2O_{6.8}$-2%GR.

3.3. FT-IR analysis

FT-IR spectra of GO, $Cd_2Sb_2O_{6.8}$-GR and pure $Cd_2Sb_2O_{6.8}$ were shown in Fig. S2. As shown in Fig. S2, the characteristic peaks of GO were the adsorption peaks C=O stretching vibration of the COOH groups (1720 cm^{-1}), the C—O stretching vibration of the epoxy groups (1050 cm^{-1}), the C—OH stretching at 1224 cm^{-1} and the sp^2 character at 1620 cm^{-1} [35,30,31]. It could be evidently seen that almost all the characteristic bands of GO disappeared, suggesting that GO in $Cd_2Sb_2O_{6.8}$-GR composites had fully been reduced.

3.4. XPS analysis

XPS was a surface analytical technique that could provide useful information on the characteristic of the functional groups and the chemical constituents of surface. To find out the difference among pure GR, $Cd_2Sb_2O_{6.8}$ and their composite, the C1s spectra of these could be deconvoluted into different peaks (Fig. S3). The carbon peaks of bare $Cd_2Sb_2O_{6.8}$ derived from carbonaceous impurities. The C1s spectra of $Cd_2Sb_2O_{6.8}$ and pure GR could be deconvoluted into different peaks (Fig. S3b and S3c). Specifically, when compared the $Cd_2Sb_2O_{6.8}$, GR and $Cd_2Sb_2O_{6.8}$-GR (Fig. S3a), the peak of C1s which attributed to the epoxy group (C—O—C, 286.7 eV) in bare $Cd_2Sb_2O_{6.8}$ photocatalyst was died out. However, a significant epoxy groups existed in GR and $Cd_2Sb_2O_{6.8}$-GR samples, due to the epoxy group which was not completely reduction of GO. So there was being epoxy groups in GR and $Cd_2Sb_2O_{6.8}$-GR photocatalysts, which distinguished from pure $Cd_2Sb_2O_{6.8}$. This property might improve the ability of photocatalytic degradation for $Cd_2Sb_2O_{6.8}$-GR photocatalysts.

The XPS spectra of $Cd_2Sb_2O_{6.8}$ and $Cd_2Sb_2O_{6.8}$-GR, before and after photocatalytic degradation of RhB, are shown in Figs. S5a and S6a. It was found that the main peaks were a result of elements of Cd, Sb and O. The comparisons of these are discussed in section of photocatalytic stability of $Cd_2Sb_2O_{6.8}$-GR nanocomposites.

3.5. Optical properties

The UV–vis DRS of $Cd_2Sb_2O_{6.8}$-GR, pure $Cd_2Sb_2O_{6.8}$ and commercial P25 were shown in Fig. S4. As can be seen clearly, there was no significant absorption for pure $Cd_2Sb_2O_{6.8}$ in the region 420–800 nm, while $Cd_2Sb_2O_{6.8}$-GR had much stronger absorptive capacity in the whole visible region due to the presence of GR. It is well known that the formula $[F(R)E]^2 = A(E - Eg)$ could describe the relation between the absorption coefficient and band gap energy of direct-gap semiconductor, while E and E_g were the photon energy and optical band gap energy, respectively. A respected the characteristic constant of semiconductors. When extrapolated the linear relation to $[F(R)E]^2 = 0$ give the band gap E_g of the sample, as shown in Fig. S4 (inset). For pure $Cd_2Sb_2O_{6.8}$ the band gap energy can be

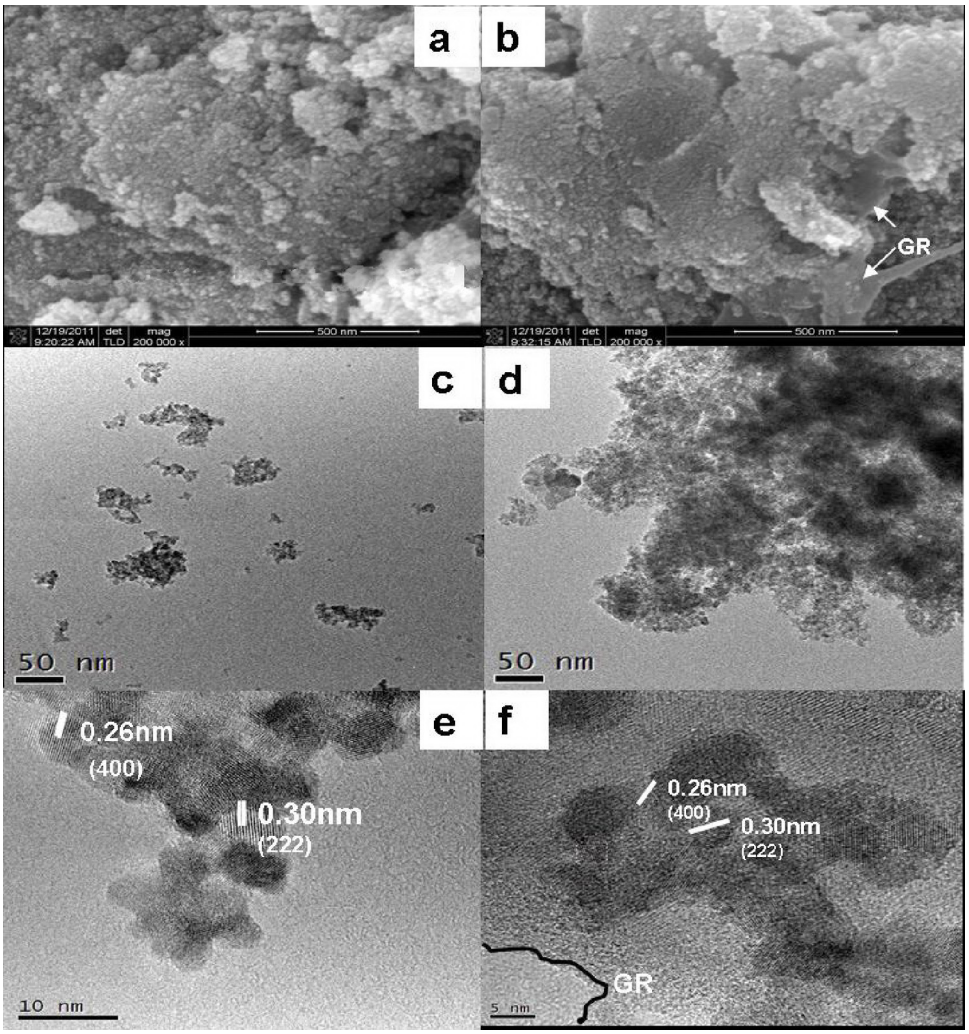

Fig. 3. The SEM, TEM and HRTEM images of pure $Cd_2Sb_2O_{6.8}$ and $Cd_2Sb_2O_{6.8}$-2%GR nanocrystallines: (a) SEM, (c) TEM and (e) HRTEM of $Cd_2Sb_2O_{6.8}$; (b) SEM (d) TEM and (f) HRTEM of $Cd_2Sb_2O_{6.8}$-2%GR.

estimated as 3.9 eV. Unfortunately, for the $Cd_2Sb_2O_{6.8}$-GR system, the band gap energy was difficult to be estimated from the DRS data. After characterized by the above tests, we could make sure that GR sheets and the semiconductor $Cd_2Sb_2O_{6.8}$ had been integrated by a way of effective contact. It was further evidenced by SEM, TEM and HRTEM as shown in Fig. 3.

3.6. Morphology measurement

Fig. 3(a), (c) and (e) shows the patterns of SEM, TEM and HRTEM of pure $Cd_2Sb_2O_{6.8}$, while Fig. 3(b), (d) and (f) showed the SEM, TEM and HRTEM of $Cd_2Sb_2O_{6.8}$-2%GR, respectively. Fig. 3(c) and (d) TEM images showed that when GR sheets were used as support, they were densely decorated by $Cd_2Sb_2O_{6.8}$ nanoparticles, which was consistent with the SEM results (Fig. 3(b)). What's important was that almost no particles scattered out of GR scaffolding as shown in Fig. 3(d). It indicated a strong interaction between the particles and GR sheets. The HRTEM image (Fig. 3(e)) showed that these nanoparticles had an average diameter of 5–10 nm. Consistent with the results of Sun et al. [7], the clearly observed lattice spacing of 0.30 nm and 0.26 nm corresponded to the (2 2 2) and (4 0 0) crystal planes of $Cd_2Sb_2O_{6.8}$ respectively. The typical lattice spacing of $Cd_2Sb_2O_{6.8}$ was also been observed distinctly in the $Cd_2Sb_2O_{6.8}$-2%GR images (shown in Fig. 3(f)). In addition, we could even notice that the $Cd_2Sb_2O_{6.8}$ particles and GR strongly combined with each other. As we all know, GR sheets were extremely thin, it is difficult to make a distinction between them and the carbon-supported film on the copper grid [36]. Compared with the bright and dark field as HRTEM images showed in Fig. 3(e) and (f), the GR sheets could be distinguished from the background. And also, we can identify the outline of GR sheets showed in the TEM image (Fig. 3(d)). Moreover, through the analyses by Raman, FT-IR, DRS and XRD, it is believed that these $Cd_2Sb_2O_{6.8}$ nanoparticles deposited on the GR sheets firmly. Thus, according to the above experimental results, $Cd_2Sb_2O_{6.8}$-GR nanocomposites were obtained.

3.7. Tests of photocatalytic activity

3.7.1. Photocatalytic activity of $Cd_2Sb_2O_{6.8}$-GR nanocomposites

The liquid-phase photocatalytic activities of $Cd_2Sb_2O_{6.8}$ and $Cd_2Sb_2O_{6.8}$-GR were measured by the photocatalytic degradation of RhB and MB. As a reference, the photocatalytic behavior of Degussa P25 (TiO_2) was also measured in the same conditions.

Fig. 4(a) shows the profile of the photocatalytic degradation efficiency of RhB for $Cd_2Sb_2O_{6.8}$, $Cd_2Sb_2O_{6.8}$-GR and P25 under UV light irradiation ($\lambda = 254$ nm) at room temperature. The normalized interim concentration changes (C/C_0) of RhB during the photocatalytic degradation process were measured by the normalized maximum absorbance changes (A/A_0) of RhB at 554 nm after a given time interval. As Fig. 4(a) showed that the concentration

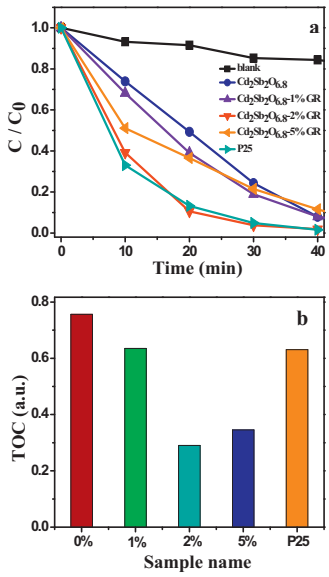

Fig. 4. Photodegradation of RhB catalyzed by $Cd_2Sb_2O_{6.8}$ and $Cd_2Sb_2O_{6.8}$-GR with different GR contents under UV light irradiation (λ = 254 nm). (a) Variation of normalized C/C_0 for RhB (C_0: the initial RhB concentration after adsorption equilibrium, C is the concentration of RhB at time t). (b). The total organic carbon (TOC) residual quantity of RhB over different catalysts after photodegradation 40 min. The sample name express that $Cd_2Sb_2O_{6.8}$–xGR (x = 0% (pure $Cd_2Sb_2O_{6.8}$), 1%, 2%, 5%).

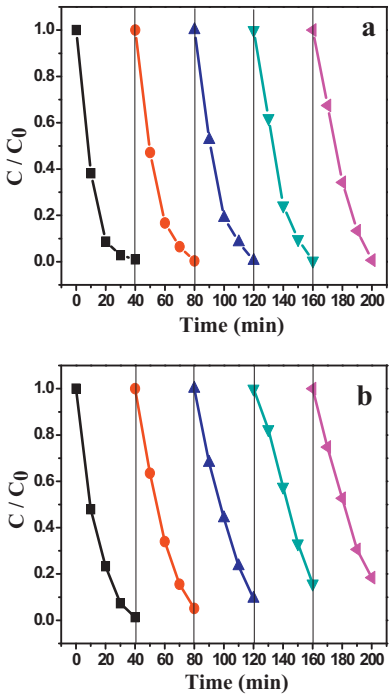

Fig. 5. Photodegradation stability of RhB over (a) $Cd_2Sb_2O_{6.8}$-2%GR and (b) $Cd_2Sb_2O_{6.8}$ nanocomposites under UV irradiation (λ = 254 nm).

of RhB was degradated by only 15.6% for the blank sample (only photodegradation) after 40 min irradiation. The photocatalytic degradation ratio of RhB for $Cd_2Sb_2O_{6.8}$-2%GR nanocomposites was 98.1% (almost as well as P25 = 98.4%) during the same irradiation time, which exceeded that for pure $Cd_2Sb_2O_{6.8}$ (92.1%), $Cd_2Sb_2O_{6.8}$-1%GR (92.0%) and $Cd_2Sb_2O_{6.8}$-5%GR (88.5%). However, the pure $Cd_2Sb_2O_{6.8}$ exhibited relatively lower photocatalytic degradation efficiency than the $Cd_2Sb_2O_{6.8}$-GR composites during the first 30 min of irradiation. The result clearly indicated that the introduction of GR could improve the ability of $Cd_2Sb_2O_{6.8}$ to photocatalytic degradation the organic pollutants and $Cd_2Sb_2O_{6.8}$-2%GR with the optimum ratio of GR had the best photocatalytic activity. Remarkably, the degradation efficiency of RhB over $Cd_2Sb_2O_{6.8}$-2%GR was almost as good as that of Degussa P25, which was usually used as an evaluation standard of photocatalysts.

Moreover, to investigate the mineralization of the RhB molecules in the photocatalytic oxidation process, the residual quantity of TOC has been measured under UV irradiation (λ = 254 nm) and showed in Fig. 4(b). The results indicated that the organic pollution RhB were degraded and mineralized. The residual quantity of TOC for $Cd_2Sb_2O_{6.8}$ (75.7%) was much larger than that for $Cd_2Sb_2O_{6.8}$-GR (1% (63.5%), 2% (29.0%), 5% (34.6%)), which reconfirmed that the introduction of GR made the $Cd_2Sb_2O_{6.8}$-GR composites exhibited a higher mineralization ability than pure $Cd_2Sb_2O_{6.8}$. Notablely, we also founded that the residual quantity of TOC for $Cd_2Sb_2O_{6.8}$-2%GR (29.0%) was even lower than that for P25 (63.1%) under the same irradiation conditions. Its implying that $Cd_2Sb_2O_{6.8}$-2%GR was a more efficient photocatalyst than P25 at the aspect mineralization for photocatalytic degradation of RhB.

As all we know, the ratio of GR in the GR-based composites has important influence for the photocatalytic activity. To further evaluate photocatalytic performance of $Cd_2Sb_2O_{6.8}$-GR composites, MB was chosen as another representative pollutant. As displayed in Fig. S8, the $Cd_2Sb_2O_{6.8}$-GR composite photocatalytic degradation efficiency of MB under UV (λ = 254 nm) light follows the order $Cd_2Sb_2O_{6.8}$-2%GR > $Cd_2Sb_2O_{6.8}$-5%GR > $Cd_2Sb_2O_{6.8}$-1%GR > pure $Cd_2Sb_2O_{6.8}$. By comparing the photocatalytic activity of P25 and $Cd_2Sb_2O_{6.8}$-2%GR, we found that although the photocatalytic rate of $Cd_2Sb_2O_{6.8}$-2%GR was slight slower than P25 but they almost can complete degradation of MB within the same 30 min.

Obviously $Cd_2Sb_2O_{6.8}$-2%GR owned the best photocatalytic degradation ability among all of the $Cd_2Sb_2O_{6.8}$-GR nanocomposites for degradation of both RhB and MB dyes. As a consequence, the $Cd_2Sb_2O_{6.8}$-2%GR with the optimum ratio of GR presented the highest photocatalytic degradation efficiency in our composite systems. So, it was crucial to control the addition proportion of GR in order to achieve the best synergy interaction between the catalyst and GR.

3.7.2. *Photocatalytic stability of $Cd_2Sb_2O_{6.8}$-GR nanocomposites*

For the practical application as a photocatalyst, the photocatalytic stability and reuse were essential parameters. $Cd_2Sb_2O_{6.8}$-2%GR was chosen to further evaluate its stability due to its outstanding activity among a variety of $Cd_2Sb_2O_{6.8}$-GR nanocomposites. We repeated activity test for five times to evaluate the activity stability by reuse of the photocatalyst with adding the same quantity of fresh RhB after each run. The results were shown in Fig. 5. From Fig. 5(a), we concluded that although the degradation rate of $Cd_2Sb_2O_{6.8}$-2%GR was slightly reduced within the first 30 min but it can be almost completely degradated in the whole process toward RhB. As a reference, we also tested the photocatalytic stability of pure $Cd_2Sb_2O_{6.8}$ (Fig. 5(b)). The experiments showed that $Cd_2Sb_2O_{6.8}$ showed a little inactivation when contrasted with $Cd_2Sb_2O_{6.8}$-2%GR nanoparticles in the entire process. The XRD patterns of $Cd_2Sb_2O_{6.8}$ and $Cd_2Sb_2O_{6.8}$-2%GR before and after reaction with RhB were shown in Fig. S7. The XRD patterns showed nearly the same, indicating that the crystal phase of $Cd_2Sb_2O_{6.8}$ and $Cd_2Sb_2O_{6.8}$-2%GR had no obvious change. This phenomenon instructed that it would be helpful to improve the photocatalytic stability of $Cd_2Sb_2O_{6.8}$ catalysts when effectively loaded on GR.

By comparing the XPS spectra of $Cd_2Sb_2O_{6.8}$ and $Cd_2Sb_2O_{6.8}$-GR, before and after photodegradation of RhB (shown in Figs. S5a and S6a.), it was found that the main peaks were a result of elements

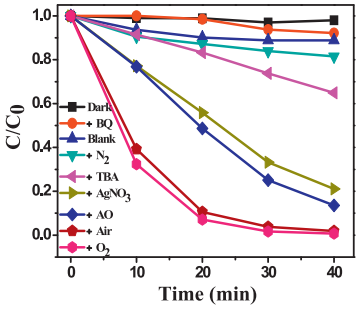

Fig. 6. Photocatalytic degradation of RhB over $Cd_2Sb_2O_{6.8}$-2%GR with exposure to UV light (λ = 254 nm): in the dark (have catalysts without irradiation), adding BQ, Blank (irradiated without catalysts), N_2-saturated, adding TBA, adding $AgNO_3$, adding AO, air-equilibrated and O_2-saturated.

of Cd, Sb and O. What's more, the binding energies of Cd3d and Sb3d of these used samples had no obvious charge shifts as contrast with those of fresh (Figs. S5b, S5c and S6b, 6c). This indicated the crystal structure and chemical state stability of $Cd_2Sb_2O_{6.8}$ and $Cd_2Sb_2O_{6.8}$-GR photocatalysts. However, the peaks intensity of $Cd_2Sb_2O_{6.8}$ and $Cd_2Sb_2O_{6.8}$-GR after photocatalytic reaction has been reduced somewhat, but the decreasing extent of $Cd_2Sb_2O_{6.8}$-GR (Fig. S6b and S6c) was far less than that of pure $Cd_2Sb_2O_{6.8}$ (Fig. S5b and S5c). The diminished peaks mean the loss of the active ingredients, which might be the reason that led to the deactivation of pure $Cd_2Sb_2O_{6.8}$. As for $Cd_2Sb_2O_{6.8}$-GR composites, due to the presence of GR, $Cd_2Sb_2O_{6.8}$ nanoparticles could be fixed on the surface of GR tightly, GR act as an effect of protection in here. So these combinations prevented the loss of active ingredients efficiently, thus $Cd_2Sb_2O_{6.8}$-GR had obviously improved photocatalytic stabilities.

4. Discussion of photocatalytic mechanism

4.1. Detection of active species by scavengers

We know that the photocatalytic reaction mechanism and the active species were closely related with each other. As to investigate the active species which might exist in the photodegradation process, different types of active species scavengers were added in the catalytic system. Fig. 6 shows the photocatalytic activities of $Cd_2Sb_2O_{6.8}$-2%GR in the degradation of RhB under different conditions. The main absorption peak at 554 nm of RhB was selected to analyze the photocatalytic conversion ratio (PCR) data. As shown in Fig. 6, without the addition of any scavengers, the PCR of RhB on $Cd_2Sb_2O_{6.8}$-2%GR was 98% after 40 min of irradiation. Usually, the separation of electrons and holes were recognized to be very important in the initial step of photodegradation mechanism [37]. Therefore, scavengers for electrons and holes were employed to determine the specific reactive species. As a kind of electron scavenger, $AgNO_3$ was added to the system, the PCR was reduced to 79%. The decrease of the amount of electrons could possibly reduce the generation of active species such as $\cdot O_2^-$ then inhibit the degradation rate. To determine the role of holes, ammonium oxalate (AO) as a hole-scavenger was added into the reaction system [38], the PCR was remarkably reduced to 86%. The rate for degradation of RhB was inhibited by the decrease of the amount of holes. Therefore, the conclusion was that both of electrons and holes all had an effect on the degradation process.

The ·OH and $\cdot O_2^-$ radicals were reported to be the main active species in many catalytic reactions [39]. When two milliliters of tert-butyl alcohol (TBA) as a scavenger of ·OH radicals was added to the solution, as mentioned in Fig. 6. The PCR was reduced to 35%. The benzoquinone (BQ) was added to determine the $\cdot O_2^-$. As BQ has the ability to trap $\cdot O_2^-$ by a simple electron transfer mechanism (Eq. (1)) [38]. The addition of BQ (0.08 g) largely suppressed the degradation rate and the PCR was reduced to 8%. What is surprising was that the addition of BQ made the photocatalytic activity inhibited severely and the PCR was even lower than the RhB blank (11%) (photodegradation). The addition of BQ and TBA had fully demonstrated that $\cdot O_2^-$ and ·OH played an important role in the photocatalytic process.

$$BQ + {}^{\bullet}O_2^- \rightarrow BQ^{\bullet -} + O_2 \quad (1)$$

As shown in Fig. 6. The reaction rate was also markedly accelerated under the state of oxygen enrichment the PCR in this situation was 100%. While in air-equilibrated was 98%. It seemed that dissolved O_2 played an essential role in the degradation process. So, to test the role of the dissolved O_2 in the reaction system, N_2 (10 mL/min) was bubbled into the suspensions to make sure the reaction was carried out under anaerobic conditions. As shown in Fig. 6, after the exclusion of oxygen, the photodegradation was strongly inhibited and the PCR was significantly reduced to 18%. In other word, dissolved O_2 was essential on the degradation process.

We have proposed that the holes could reacted with the surface hydroxyl and water of suspension to produce ·OH in our previous work [38]. As mentioned in Fig. 6, we noticed that after adding AO to the reaction system, the PCR was reduced to 86%. But once TBA was added, it can reduce to the PCR to 35%. That is to say, the source of produced hydroxyl radical was more than just the holes. In order to verify the above conclusion, the generation of ·OH radicals was investigated by the photoluminescence (PL) technique in p-phthalic acid (TA) suspension (PL-TA) [40]. Fig. S9 showed changes of PL signals in the presence of $Cd_2Sb_2O_{6.8}$-2%GR under different conditions (blank, adding AO, adding TBA). As we could see, the generation of ·OH had a different degree of inhibition by adding AO and TBA. However, the inhibition caused by AO was obviously weaker than that of TBA. In other words, there must be other species, which can produce the ·OH radicals in the photocatalytic process.

4.2. Detection of active species

4.2.1. Detection of ·OH and $\cdot O_2^-$ radicals

To further confirm the existence of the active species and make sure whether the introduction of GR could have some impacts on the generation of active species. The following characterizations were carried out. The PL technique with TA as a probe molecule was used in the detection to investigate the generation of ·OH [38], as shown in Fig. S10. In $Cd_2Sb_2O_{6.8}$-2%GR systems, the PL intensity increased steadily within 40 min of irradiation. It meant that the ·OH radicals were proportional to the light irradiation time.

Next, the generation of both ·OH and $\cdot O_2^-$ radicals were then confirmed by the spin-trapping ESR technique [41]. Under the point source of 254 nm irradiation in the same time, four stronger and more visible characteristic peaks with intensity 1:2:2:1 for DMPO-•OH species were observed over $Cd_2Sb_2O_{6.8}$-2%GR than that of pure $Cd_2Sb_2O_{6.8}$, as shown in Fig. 7(a). Similar tendency of enhancement was also observed for the DMPO-$^{\bullet}O_2^-$ species, as per Fig. 7(b) shown. In conclusion, the formation rates of •OH and $^{\bullet}O_2^-$ radicals on $Cd_2Sb_2O_{6.8}$-2%GR were much higher than that of pure $Cd_2Sb_2O_{6.8}$.

4.2.2. Detection of H_2O_2 species

H_2O_2 was another important intermediate species in the photocatalysis process, DPD method was usually employed to detect it. As illustrated in Fig. 8. When a sequential addition of DPD and POD to the suspension, more hydrogen peroxide radicals were tested in the $Cd_2Sb_2O_{6.8}$-2%GR reaction system. What this supposed to mean was that the system had more strong ability to produce hydrogen peroxide due to the introduction of GR. To sum up, significant

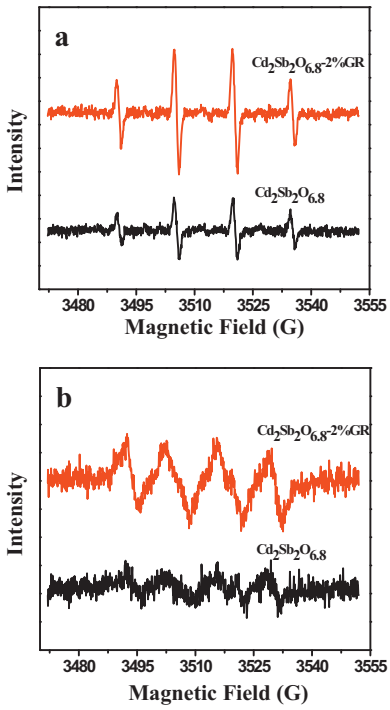

Fig. 7. DMPO spin-trapping ESR spectra for $Cd_2Sb_2O_{6.8}$ and $Cd_2Sb_2O_{6.8}$-2%GR (under the point source light of 254 nm, within the same irradiation time): (a) in aqueous dispersion for DMPO-•OH and (b) in methanol dispersion for DMPO-•O_2^-.

changes occurred in the amount of active species due to the presence of GR in the $Cd_2Sb_2O_{6.8}$-2%GR systems. This corresponds to the results that $Cd_2Sb_2O_{6.8}$-2%GR owned a higher photocatalytic activity than pure $Cd_2Sb_2O_{6.8}$ toward the degradation of organic dyes.

4.3. Relationship between the active species and the degradation

4.3.1. LC–MS detection

To probe the main byproducts of RhB and to investigate whether the dope of GR would cause different degradation process, LC-MS technique was applied. Fig. S11 and Fig. S12 reported chromatogram corresponding to solution of RhB degraded by $Cd_2Sb_2O_{6.8}$-2%GR and $Cd_2Sb_2O_{6.8}$, respectively. As shown in these two pictures, without UV irradiation, there was only one peak

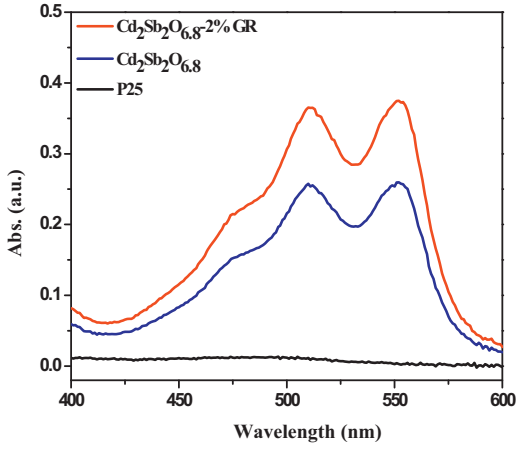

Fig. 8. Detection of H_2O_2 in $Cd_2Sb_2O_{6.8}$ and $Cd_2Sb_2O_{6.8}$-2%GR water dispersions (0.06 g/150 mL) under 254 nm light irradiation, Curves were obtained by addition of DPD and POD to the dispersions after 40 min of irradiation.

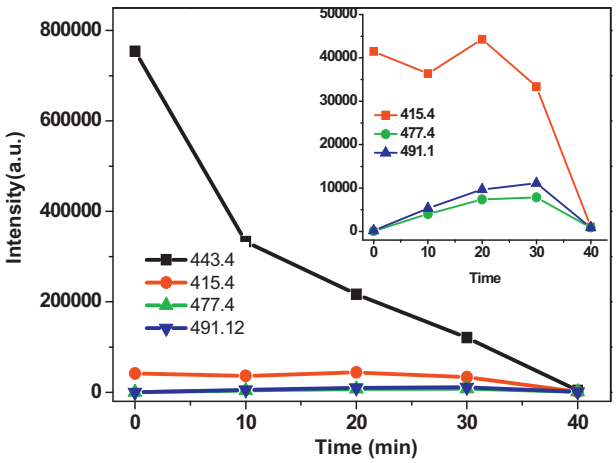

Fig. 9. Mass spectrum view changes of the peak intensity appeared in photocatalytic process of $Cd_2Sb_2O_{6.8}$-2%GR system.

appeared at 12.3 min, which belongs to the RHB molecule. However, after 10 min of UV irradiation, several peaks which classified to byproducts were observed. With the light irradiation, the intensity of the peak quickly decreased and finally its intensity reached a minimum. Similar situation were observed in both of $Cd_2Sb_2O_{6.8}$-2%GR and $Cd_2Sb_2O_{6.8}$ chromatogram. Fig. S11 and Fig. S12 also provided the corresponding mass spectra of the degradation byproducts. Significant mass peaks were labeled with the corresponding m/z values. In the process of degradation on $Cd_2Sb_2O_{6.8}$-2%GR, five strong mass peaks (m/z = 443, 415, 491, 477 and 282) had been observed, while seven strong mass peaks (m/z = 443, 415, 459, 477, 387, 491 and 282) appeared on $Cd_2Sb_2O_{6.8}$. What is noticeable was that $Cd_2Sb_2O_{6.8}$-2%GR has fewer byproduct peaks observed in the same time interval than pure $Cd_2Sb_2O_{6.8}$. This is because the system of $Cd_2Sb_2O_{6.8}$-2%GR had a stronger degradation capability than $Cd_2Sb_2O_{6.8}$. According to the LC–MS analysis and the structure of RhB, we inferred possible structures of degradation byproducts and pathways of photodegradation in Fig. S13. We had to point out that the inferred degradation fragments of RhB might have many isomeric compounds and the mechanism we have proposed was a most likely one based on experiments.

The changes of mass spectrum intensity of different fragments could indicate how the degradation processes carried out. So we tested changes of the intensity of these main byproducts. Fig. 9 showed the changes of mass spectrum intensity of main peaks m/z = 443, 415, 477 and 491 appeared at different retention time in the process of $Cd_2Sb_2O_{6.8}$-2%GR system. There were three kinds of main byproducts in the degradation process. One of which was m/z = 415 appearing in the time of 11.3 min. Its intensity increased in the first 20 min, and then started to decrease. This is because at the first 20 min, the rate of generated this fragments was faster than the rate of its decomposition. As the reaction of degradation, in the last 20 min, the concentration of the byproduct was reduced and accelerated the decomposition rate. The fragments of m/z = 477 and 491 had a similar phenomenon. The changes of the intensity of these byproducts were explained in Note 3 (see Supporting Information).

4.3.2. ORP and conductivity detection

The photodegradation process was also detected in situ by the ORP and conductivity electrodes. Fig. 10 shows the changes of ORP and conductivity in the degradation process of RhB. These two electrodes could detect the degradation process in situ, which verify the results detected by LC–MS. As shown in Fig. 10 the values of

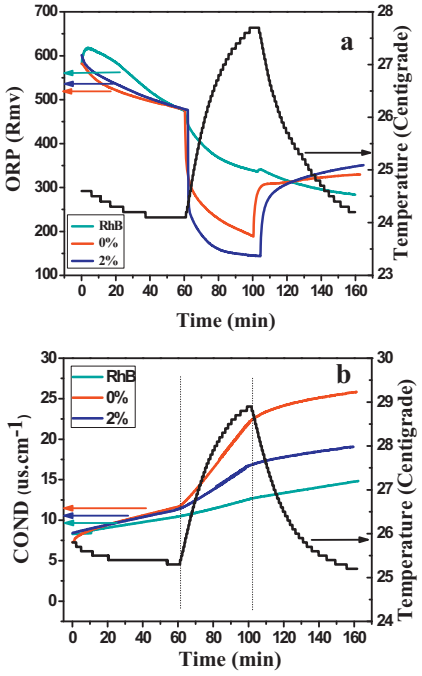

Fig. 10. Changes of (a) ORP and (b) the conductivity (COND) during $Cd_2Sb_2O_{6.8}$-2%GR (2%) and $Cd_2Sb_2O_{6.8}$ (0%) photocatalysts in aqueous RhB suspension.

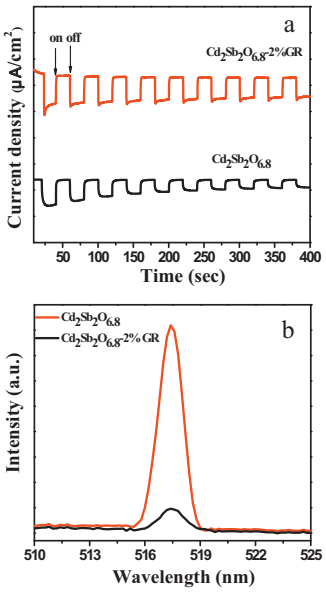

Fig. 11. (a) Photocurrent transient responses of $Cd_2Sb_2O_{6.8}$ and $Cd_2Sb_2O_{6.8}$-2%GR electrodes under UV irradiation ($\lambda = 254$ nm), [$NaSO_4$] = 0.1 mol/L. (b) The photoluminescence (PL) spectra of $Cd_2Sb_2O_{6.8}$ and $Cd_2Sb_2O_{6.8}$-2%GR nanocomposite (Ex = 322 nm).

the ORP and conductivity of RhB remain stable in dark, when the light irradiation, the values were quickly reduced in the first 10 min and then the changes slow down. After 40 min of light irradiation, the values became stable. The value increased again when the light turned off.

We can explain this phenomenon from the transfer of electrons and the generation of active species during the photodegradation process. While in the dark, there were no electrons generated in the system, so the values of ORP were kept stable. As the light irradiation, the photoelectrons started to be generated on the surface of catalysts. Then active species were generated in the following reactions. With the degradation of RhB and the production of its byproducts, the ORP value changed. It was difficult to ensure the clear redox couples which induced the changes of ORP values. But the change trends could show us how the degradation carried out under the effect of the active species.

Changes of mass spectra intensity (Fig. 9) echoed well with this phenomenon. During the first 10 min of light irradiation, the changes of the degradation product were quickly carried out. Accordingly, during this time, the ORP had a large turn and the conductivity increased sharply. Since then, the following reactions were not so fast any more. But there were still active species and byproducts generated in the process. So the conductivity was increased all the time. As the light was off, there were no photogenerated electrons and the concentration of byproducts was low. So the conductivity and ORP value trend to be relatively stable. The changes of conductivity and ORP were largely depended on the active species and the byproducts in this degradation process, due to the changes of temperature during this process almost as the same.

Notablely, the changes of ORP and conductivity for $Cd_2Sb_2O_{6.8}$-2%GR was more obvious than $Cd_2Sb_2O_{6.8}$. We explain this phenomenon for the reason that, there were more photogenerated electrons participating in the redox reaction since the GR in $Cd_2Sb_2O_{6.8}$-2%GR nanocomposites played a role of electron conveyor. These led to the improvement of the degradation rate. All of this could be verified by the LC–MS chromatogram.

4.4. Role of graphene in the degradation process

4.4.1. Analysis of specific surface area

As we know, the specific area of material was closely related to the photocatalytic activity. During the photodegradation process, a large specific surface area was in favor of accelerating the reaction rate. As shown in Table 1, it is clearly shown that the specific surface area was in direct proportion with the amount of the introduced GR. The BET specific surface area of $Cd_2Sb_2O_{6.8}$-2%GR was determined to be 147.8 $m^2\,g^{-1}$, which was much smaller than that of $Cd_2Sb_2O_{6.8}$-5%GR (160.8 $m^2\,g^{-1}$). However, $Cd_2Sb_2O_{6.8}$-2%GR owned the best photocatalytic activity in all the samples (shown in Fig. 4 and Fig. S8). This indicated that the improvement of GR content in the photocatalysts might exist a relationship with the enhanced surface area. However, after careful analysis of the data, we had come to the results that the specific surface area was not the only crucial factors which affected the photocatalytic activity caused by GR. There must be some other effects of GR influenced the reaction mechanism.

4.4.2. Detection of interface charge separation efficiency

As is known to all, the separation of electrons and holes was recognized to be the initial step in the photodegradation mechanism. The interface charge separation efficiency could be disclosed by photocurrent spectra [24] and PL spectra [30,42]. Fig. 11(a) shows the transient photocurrent responses under intermittent UV light illumination ($\lambda = 254$ nm) for pure $Cd_2Sb_2O_{6.8}$ and $Cd_2Sb_2O_{6.8}$-2%GR. The photocurrent measurements were carried out in 0.1 mol/L Na_2SO_4 aqueous solution with zero bias, by depositing on the ITO glass electrodes.

As shown in Fig. 11(a), irradiated with UV light, the photocurrent was rapidly generated and soon reached a stable value with instant illumination time, then the values were stable on the interval time (20 s). Next, when the light was turned off, the photocurrent fell down to the initial value, immediately. One point to pay special attention to was that the photocurrent of $Cd_2Sb_2O_{6.8}$-2%GR was significantly enhanced and more stable. It indicated that the photoexcited electron–hole pairs were more efficiently separated and

Table 1
BET specific area of $Cd_2Sb_2O_{6.8}$ and $Cd_2Sb_2O_{6.8}$-GR (1%, 2%, 5%) nanocomposite.

Samples	$Cd_2Sb_2O_{6.8}$	$Cd_2Sb_2O_{6.8}$-1%GR	$Cd_2Sb_2O_{6.8}$-2%GR	$Cd_2Sb_2O_{6.8}$-5%GR
S_{BET} ($m^2\ g^{-1}$)	123.8	139.7	147.8	160.8

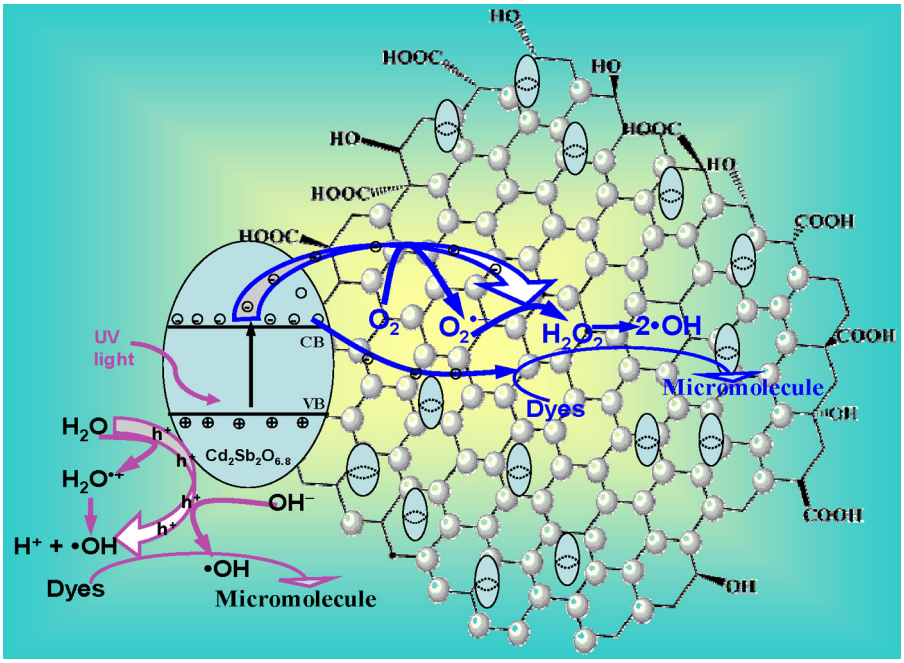

Scheme 1. Mechanism diagram of photocatalytic reaction of dyes molecules over $Cd_2Sb_2O_{6.8}$-2%GR nanocomposite under UV light.

a much longer lifetime existed in the photo-generated charge carriers since the introduction of GR.

The change in interface electron–hole separation could also be confirmed by PL spectra [24]. We know that the fluorescence emission was originated from the recombination of electrons and holes in the conduction and valence bands. Fig. 11(b) shows the transient changes in the PL spectra with the fluorescence emission maximum at 517 nm and excitation at 322 nm. As displayed in the graphic, the PL intensity obtained over $Cd_2Sb_2O_{6.8}$-2%GR was much weaker than that of pure $Cd_2Sb_2O_{6.8}$. It suggested that the recombination of photogenerated electrons and holes were extremely inhibited in $Cd_2Sb_2O_{6.8}$-2%GR. In other words, a longer lifetime of photo-generated charge carriers exists in the $Cd_2Sb_2O_{6.8}$-2%GR than pure $Cd_2Sb_2O_{6.8}$ system.

4.5. A possible photocatalytic mechanism

GR was a well-known outstanding electron acceptor and highway of electronic transmission. In the $Cd_2Sb_2O_{6.8}$-2%GR system, the photogenerated electrons of excited $Cd_2Sb_2O_{6.8}$ were injected into GR sheets instantly from the conduction band of $Cd_2Sb_2O_{6.8}$, as GR was a well accepter of electrons. The electrons could be delivered to a long distance immediately as soon as they were injected into the GR sheets. That is to say, while in the process of transferring, the electrons had more opportunities to come across and reacted with other species then to generate more active radicals. It implied that there would be more active species generated in the GR systems. In a word, based on its good electronic accept and transport property and high specific surface area of GR. It is expected to separate and deliver the generated electrons and further react with more other species to generate active radicals. The results were in good agreed with the activity tests results. On the basis of the above experimental results and analysis, a possible photocatalytic mechanism for the degradation of dyes on $Cd_2Sb_2O_{6.8}$-2%GR under UV irradiation was proposed as shown in the illustration (Scheme 1).

Under UV ($\lambda = 254$ nm) irradiation, $Cd_2Sb_2O_{6.8}$ was excited and the electron–hole pairs were generated on the $Cd_2Sb_2O_{6.8}$ catalysis. Due to GR had a good capacity of electron conduction, the electrons could be transferred from $Cd_2Sb_2O_{6.8}$ to GR sheets immediately. The more effective separation of electron–hole pairs was proved by the PL and photocurrent measurement. The electrons which were conducted to GR sheets could react with surface species to form $^{\bullet}OH$, $^{\bullet}O_2^-$ and H_2O_2. Moreover, the introduction of GR provided more opportunities to these reactions owning to its large specific surface area. The holes could react with the adsorbed water and the surface hydroxyl to form $^{\bullet}OH$ radicals. Finally, these active species such as $^{\bullet}OH$, $^{\bullet}O_2^-$, H_2O_2 and h^+ could oxidize the dye molecules which adsorbed on the surface of $Cd_2Sb_2O_{6.8}$-2%GR nanocomposites to micromolecules effectively (as shown in Scheme 1).

5. Conclusion

In summary, a series of $Cd_2Sb_2O_{6.8}$-GR nanocomposites photocatalysts was synthesized via a facial hydrothermal method. $Cd_2Sb_2O_{6.8}$-2%GR nanocomposite performed optimal activity of degrading RhB and MB under UV ($\lambda = 254$ nm) irradiation. Its photocatalytic activity toward RhB was almost as good as P25. Moreover, its TOC residual quantity implied that $Cd_2Sb_2O_{6.8}$-2%GR performed even better mineralization than P25. It found that the introduction of GR can improve both activity and stability of the catalysts. The role of GR in $Cd_2Sb_2O_{6.8}$-2%GR systems had been further discussed and founded that GR could improve the photocatalytic activity should be explained in three facets: First, GR had large specific surface area to provide more opportunities to dyes to adsorption and reaction with active species. Second, as a good electronic acceptor of GR, it could separate the electron–hole pairs efficiently. Third,

since it was the expressway of electron conductivity, it proved more opportunities to electrons to react with surface species then increased the number of radicals. A mechanism had been proposed, based on the degradation of RhB over $Cd_2Sb_2O_{6.8}$-2%GR catalysts. We hoped that this work could promote the research of not only in the aspect of catalyst activities but also in the aspect of mechanism of photocatalyst.

Acknowledgments

This work was financially supported by the NNSF of China (21173047, 21073036 and 21033003), National Basic Research Program of China (973 Program, 2013CB632405).

Appendix A. Supplementary data

Supplementary data associated with this article can be found, in the online version, at http://dx.doi.org/10.1016/j.apcatb.2013.07.063.

References

[1] Y.F. Liu, X.Q. Liu, Chinese Journal of Inorganic Chemistry 15 (1999) 293–300.
[2] T. Hitch, C.L. Honeybourne, Journal of Materials Chemistry 6 (1996) 285–288.
[3] X.Q. Liu, Y.F. Liu, Y.S. Shen, Chemical Journal of Chinese Universities 19 (1998) 837–842.
[4] Y.F. Liu, X.Q. Liu, J.J. Yu, Sensors and Actuators B 61 (1999) 208–212.
[5] F. Gao, Y.F. Liu, X.Q. Liu, Sensors and Actuators B 77 (2001) 653–656.
[6] Y.F. Liu, Y.Q. Liu, Y.S. Shen, Sensors and Actuators B 55 (1999) 9–13.
[7] M. Sun, D.Z. Li, W.J. Zhang, Z.X. Chen, H.J. Huang, W.J. Li, Y.H. He, X.Z. Fu, Journal of Physical Chemistry C 113 (2009) 14916–14921.
[8] Z. Sun, T. Hasan, F. Torrisi, D. Popa, G. Privitera, F. Wang, F. Bonaccorso, D.M. Basko, A.C. Ferrari, ACS Nano 4 (2010) 803–810.
[9] Q. Bao, K.P. Loh, ACS Nano 6 (2012) 3677–3694.
[10] Y. Wang, Y. Shao, D.W. Matson, J. Li, Y. Lin, ACS Nano 4 (2010) 1790–1798.
[11] J. Zhang, J. Yu, M. Jaroniec, J.R. Gong, Nano Letters 12 (2012) 4584–4589.
[12] Q. Xiang, J. Yu, M. Jaroniec, Journal of Physical Chemistry C 115 (2011) 7355–7363.
[13] Q. Xiang, J. Yu, M. Jaroniec, Journal of the American Chemical Society 134 (2012) 6575–6578.
[14] J. Zhu, J. He, ACS Applied Materials & Interfaces 4 (2012) 1770–1776.
[15] Y. Shim, Y. Jung, H.J. Kim, Journal of Physical Chemistry C 116 (2012) 18574–18575.
[16] H. Kim, A.A. Abdala, C.W. Macosko, Macromolecules 43 (2010) 6515–6530.
[17] T. Kuilla, S. Bhadra, D. Yao, N.H. Kim, S. Bose, J.H. Lee, Progress in Polymer Science 35 (2010) 1350–1375.
[18] R. Verdejo, M.M. Bernal, L.J. Romasanta, M.A. Lopez-Manchado, Journal of Materials Chemistry 21 (2011) 3301.
[19] J. Zhang, X.S. Zhao, Journal of Physical Chemistry C 116 (2012) 5420–5426.
[20] D.R. Dreyer, R.S. Ruoff, C.W. Bielawski, Angewandte Chemie International Edition (England) 49 (2010) 9336–9344.
[21] Z. Xiong, L.L. Zhang, J. Ma, X.S. Zhao, Chemical Communications 46 (2010) 6099–6101.
[22] J. Zhang, Z. Xiong, X.S. Zhao, Journal of Materials Chemistry 21 (2011) 3634.
[23] C. Hou, Q. Zhang, Y. Li, H. Wang, Journal of Hazardous Materials 205/206 (2012) 229–235.
[24] N. Zhang, Y. Zhang, X. Pan, X. Fu, S. Liu, Y.-J. Xu, Journal of Physical Chemistry C 115 (2011) 23501–23511.
[25] T.-F. Yeh, J.-M. Syu, C. Cheng, T.-H. Chang, H. Teng, Advanced Functional Materials 20 (2010) 2255–2262.
[26] A. Ye, W. Fan, Q. Zhang, W. Deng, Y. Wang, Catalysis Science & Technology 2 (2012) 969.
[27] Z. Mou, Y. Dong, S. Li, Y. Du, X. Wang, P. Yang, S. Wang, International Journal of Hydrogen Energy 36 (2011) 8885–8893.
[28] R.E.O.W.S. Hummers, Journal of the American Chemical Society 80 (1958) 1339.
[29] L. Jia, D.-H. Wang, Y.-X. Huang, A.-W. Xu, H.-Q. Yu, Journal of Physical Chemistry C 115 (2011) 11466–11473.
[30] Y. Fu, H. Chen, X. Sun, X. Wang, Applied Catalysis B: Environmental 111/112 (2012) 280–287.
[31] Y. Fu, X. Sun, X. Wang, Materials Chemistry and Physics 131 (2011) 325–330.
[32] C. Xu, X. Wang, Small 5 (2009) 2212–2217.
[33] N. Farhangi, R.R. Chowdhury, Y. Medina-Gonzalez, M.B. Ray, P.A. Charpentier, Applied Catalysis B: Environmental 110 (2011) 25–32.
[34] S. Stankovich, D.A. Dikin, R.D. Piner, K.A. Kohlhaas, A. Kleinhammes, Y. Jia, Y. Wu, S.T. Nguyen, R.S. Ruoff, Carbon 45 (2007) 1558–1565.
[35] C. Xu, X. Wang, L. Yang, Y. Wu, Journal of Solid State Chemistry 182 (2009) 2486–2490.
[36] C. Xu, X. Wang, J. Zhu, Journal of Physical Chemistry C 112 (2008) 19841–19845.
[37] Y. Lin, D. Li, J. Hu, G. Xiao, J. Wang, W. Li, X. Fu, Journal of Physical Chemistry C 116 (2012) 5764–5772.
[38] W. Li, D. Li, Y. Lin, P. Wang, W. Chen, X. Fu, Y. Shao, Journal of Physical Chemistry C 116 (2012) 3552–3560.
[39] K. Lv, Y. Xu, Journal of Physical Chemistry B 110 (2006) 6204–6212.
[40] T. Hirakawa, Y. Nosaka, Langmuir 18 (2002) 3247–3254.
[41] Y. Hu, Y. Cao, P. Wang, D. Li, W. Chen, Y. He, X. Fu, Y. Shao, Y. Zheng, Applied Catalysis B: Environmental 125 (2012) 294–303.
[42] J. Wang, H. Ruan, W. Li, D. Li, Y. Hu, J. Chen, Y. Shao, Y. Zheng, Journal of Physical Chemistry C 116 (2012) 13935–13943.